Supplementary Materials

Boxue Wang[1a], Xinru Zhao[1a], Huachuan Sun[a]*, Mengling Zhang[a], Mingpeng Chen[a], Guoyang Qiu[a], Tong Zhou[a], Dequan Li[a], Yuewen Wu[a], Chen Liu[a], Hang Yang[a], Qinjie Lu[a], Jianhong Zhao[a], Yumin Zhang[a], Jin Zhang[a], Hao Cui[b], Feng Liu[b], Qingju Liu[a]*

[a]National Center for International Research on Photoelectric and Energy Materials, Yunnan Key Laboratory for Micro/Nano Materials & Technology, School of Materials and Energy, Yunnan University, Kunming 650091, China.

[b]Yunnan Precious Metals Laboratory Co., Ltd., Kunming, 650106, P. R. China.

[1] These authors contributed equally to this work.

***Correspondence to:**

Dr. Huachuan Sun, National Center for International Research on Photoelectric and Energy Materials, Yunnan Key Laboratory for Micro/Nano Materials & Technology, School of Materials and Energy, Yunnan University, Kunming 650091, China.

E-mail: huachuansun@ynu.edu.cn.

Prof. Qingju Liu, National Center for International Research on Photoelectric and Energy Materials, Yunnan Key Laboratory for Micro/Nano Materials & Technology, School of Materials and Energy, Yunnan University, Kunming 650091, China.

E-mail: qjliu@ynu.edu.cn.

MATERIALS AND METHODS

Reagents

The iron (III) nitrate nonahydrate ($Fe(NO_3)_3·9H_2O$), chloroplatinic acid hexahydrate ($H_2PtCl_6·6H_2O$), commercial RuO_2, hydrochloric acid (HCl), and potassium hydroxide (KOH) were purchased from Aladdin (Shanghai, China). The commercial Pt/C (20 wt%) and absolute ethanol were purchased from Suzhou Sinero Technology Co., Ltd and Chengdu Kelong Chemical Co. Ltd. Nafion solution (5 wt%) was obtained from Sigma-Aldrich, respectively. All the chemicals were used directly. Deionized (DI) water with a resistivity of 18.2 MΩ cm^{-1} was used during the experiments.

Pretreatment of NF

To obtain clean nickel foam (NF), several pieces of NF (2 × 3 cm^2) were sequentially sonicated in 3 M HCl, ethanol, and DI water for 11, 6, and 5 min, respectively, and then air-dried at room temperature.

Characterizations

The crystal structures of Pt_{QDs}@NiFe LDH and NiFe LDH were determined by X-ray diffraction (XRD). The morphologies of Pt_{QDs}@NiFe LDH and NiFe LDH were characterized by scanning electron microscopy (SEM), transmission electron microscopy (TEM), and high-resolution transmission electron microscopy (HRTEM). The surface electronic structures and chemical compositions of Pt_{QDs}@NiFe LDH and NiFe LDH were characterized by X-ray photoelectron spectroscopy (XPS). The content of Ni, Fe, and Pt elements in Pt_{QDs}@NiFe LDH was measured by inductively coupled plasma optical emission spectrometry (ICP-OES). Oxygen vacancies (O_v) of Pt_{QDs}@NiFe LDH and NiFe LDH were determined by electron paramagnetic resonance (EPR).

Electrochemical testing

The electrochemical performance of the prepared samples was measured in a typical three-electrode system using CHI 1140C and CHI 760E electrochemical workstations. Specifically, the reference electrode, counter electrode, and working electrode were Hg/HgO, carbon rod, and the synthesized samples (1 × 1 cm^2), respectively. All electrochemical tests were conducted in a 1 M KOH solution at a sweep rate of 5 mV s^{-1}. All potentials were normalized to the reversible hydrogen electrode (RHE), and all overpotentials were 95% iR-corrected. The double-layer capacitance (C_{dl}) was calculated by measuring cyclic voltammetry (CV) at different sweep rates (20, 40, 60, 80, 100, and 120 mV s^{-1}) in the non-Faradaic region. The charge transfer resistance (Rct) was obtained by measuring electrochemical impedance spectroscopy (EIS) in the frequency range from 10000 to 0.01 Hz.

Theoretical calculations

Vienna Ab initio Simulation Package (VASP)[1] was employed to perform all of the Density functional theory (DFT) calculations based on the generalized gradient approximation (GGA)[2] and Perdew-Burke-Ernzerhof (PBE) functions[3]. The projector augmented wave (PAW) model was utilized to describe the ionic cores[4]. Taking the valence electrons into account, a plane-wave cutoff was set to be 450 eV. Additionally, the convergence energy threshold for the self-consistent calculations was set to be 10-5 eV, and the geometry optimization was carried out as the total energy convergent was less than 0.02 eV/Å.

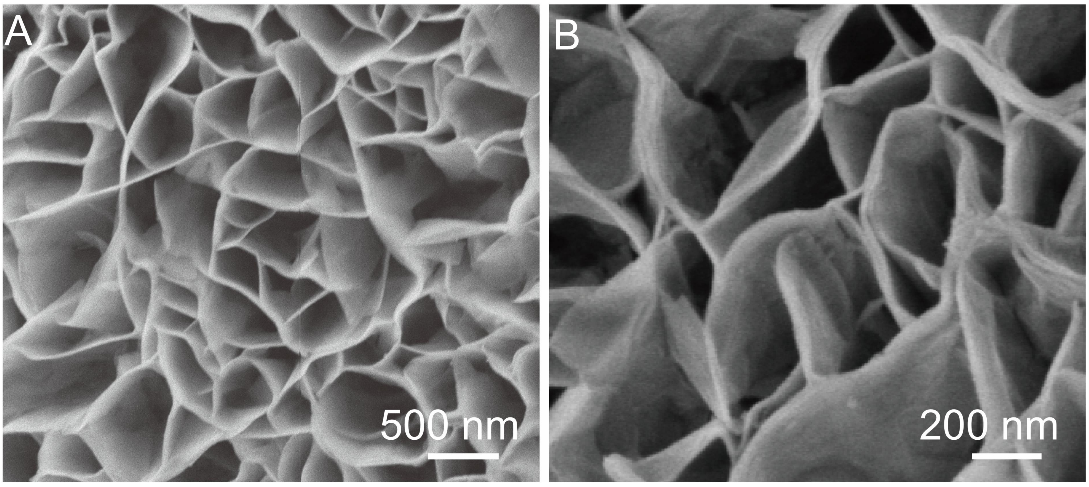

Supplementary Figure 1. (A, B) SEM images of NiFe LDH precursor at different magnifications.

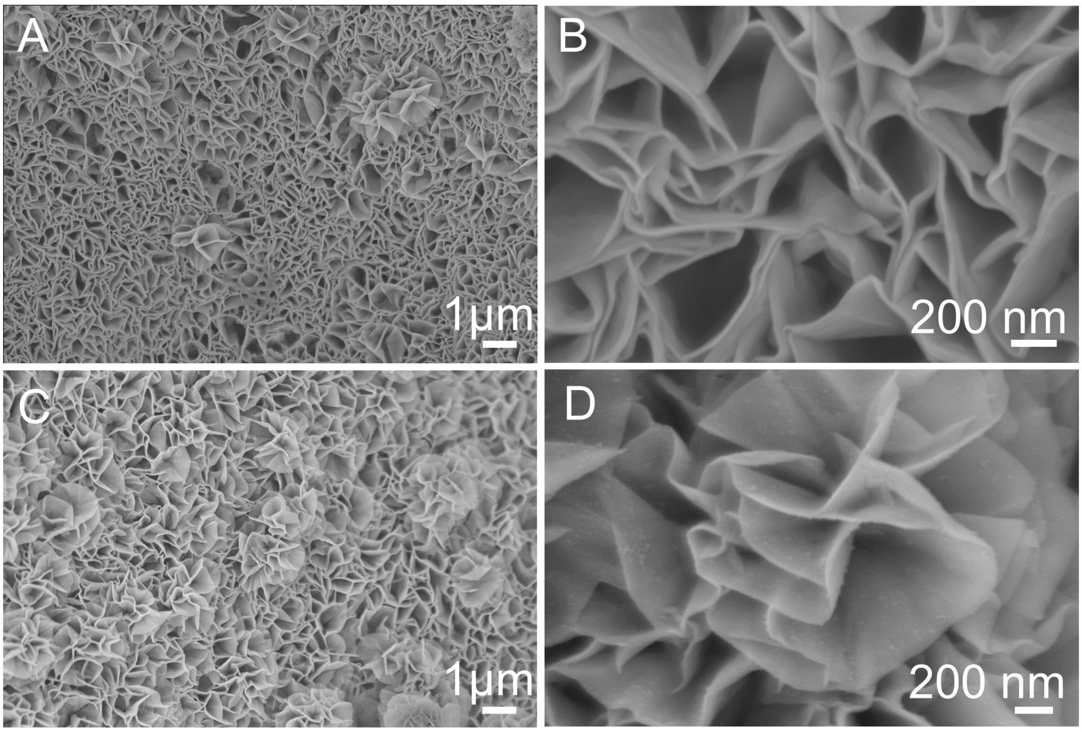

Supplementary Figure 2. (A, B) SEM images of Pt_{QDs}@NiFe LDH-1 at different magnifications. (C, D) of Pt_{QDs}@NiFe **LDH**-5 at different magnifications.

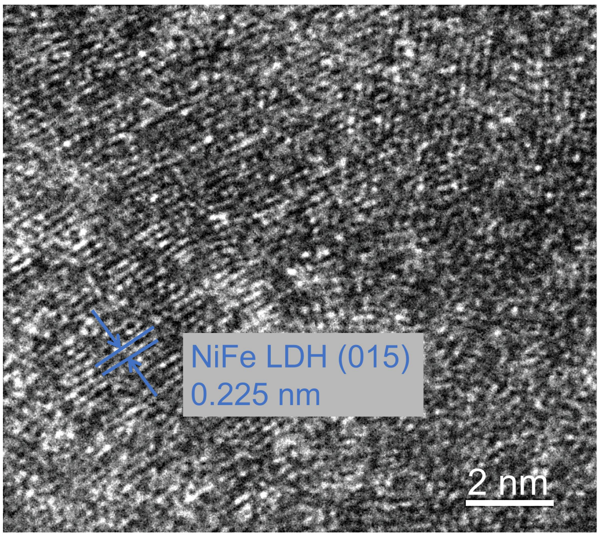

Supplementary Figure 3. HRTEM **image** of NiFe LDH.

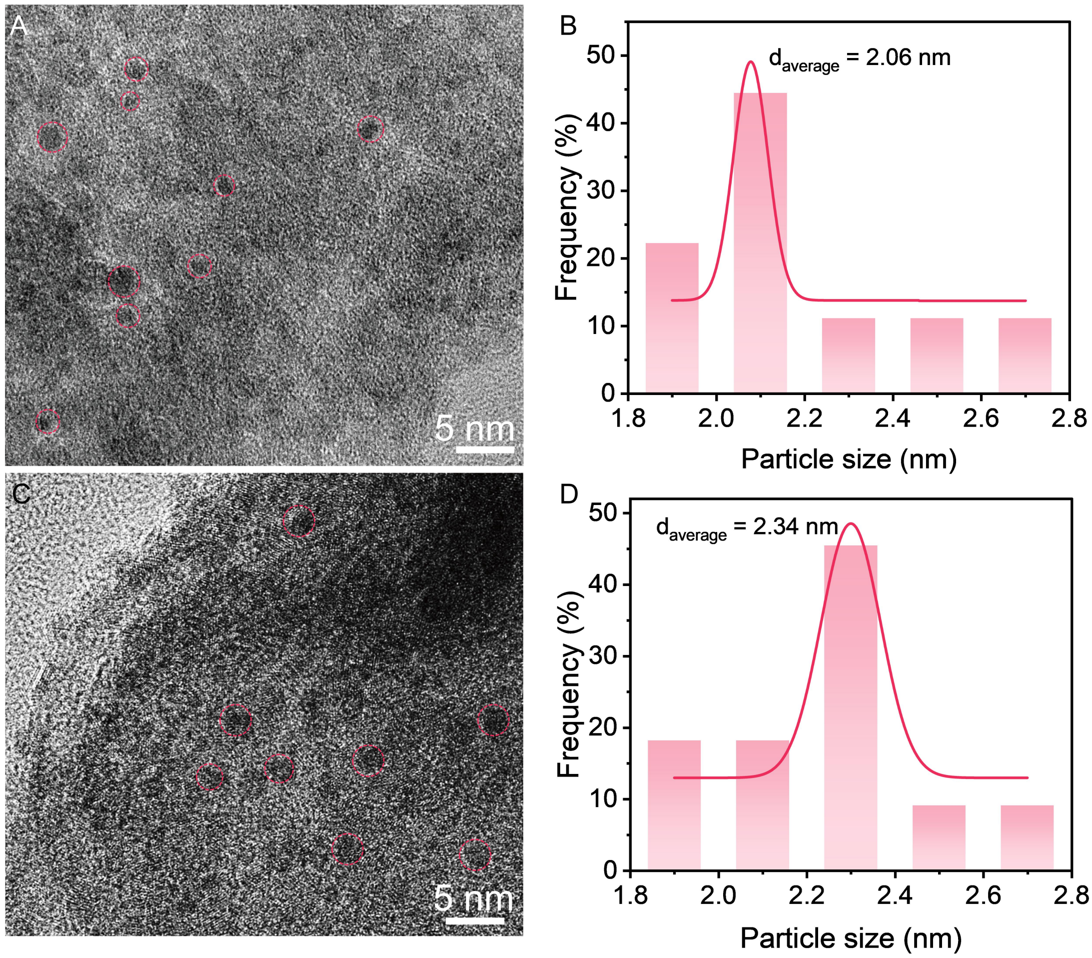

Supplementary Figure 4. (A, B) HRTEM images of Pt_{QDs}@NiFe LDH (the Pt_{QDs} are marked with pink circles) and corresponding size distribution of Pt_{QDs}. (C, D) HRTEM images of Pt_{QDs}@NiFe LDH and corresponding size distribution of Pt_{QDs}.

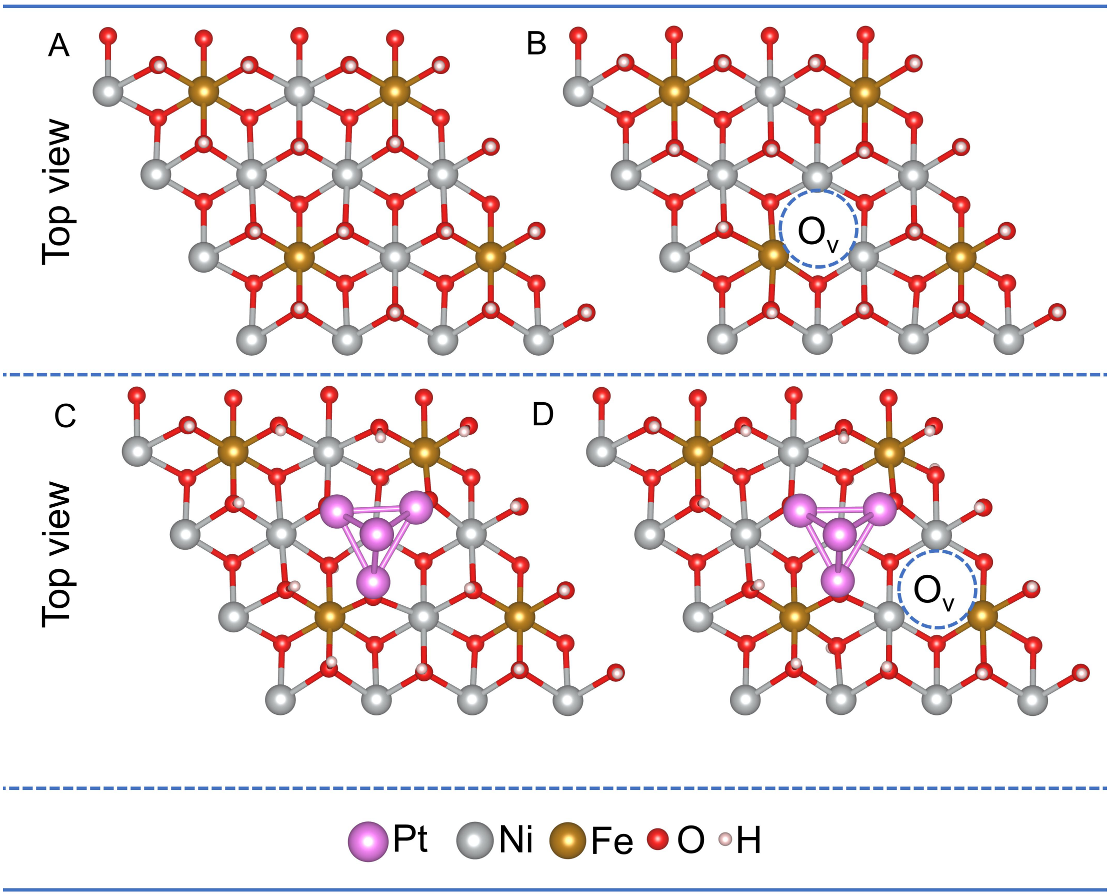

Supplementary Figure 5. The atomic models of (A) NiFe LDH without O_v, (B) NiFe LDH with O_v, (C) Pt_{QDs}@NiFe LDH without O_v, (B) Pt_{QDs}@NiFe LDH with O_v. The purple, grey, yellow, red, and pink balls represent Pt, Ni, Fe, O, and H atoms, respectively.

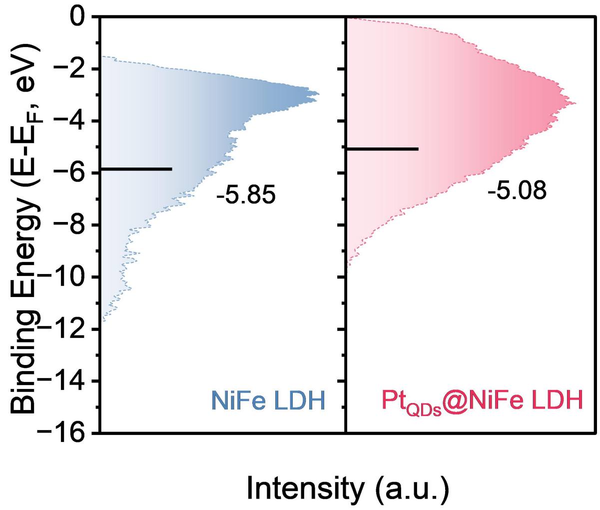

Supplementary Figure 6. Surface valence band photoemission spectra of NiFe LDH and Pt$_{QDs}$@NiFe LDH.

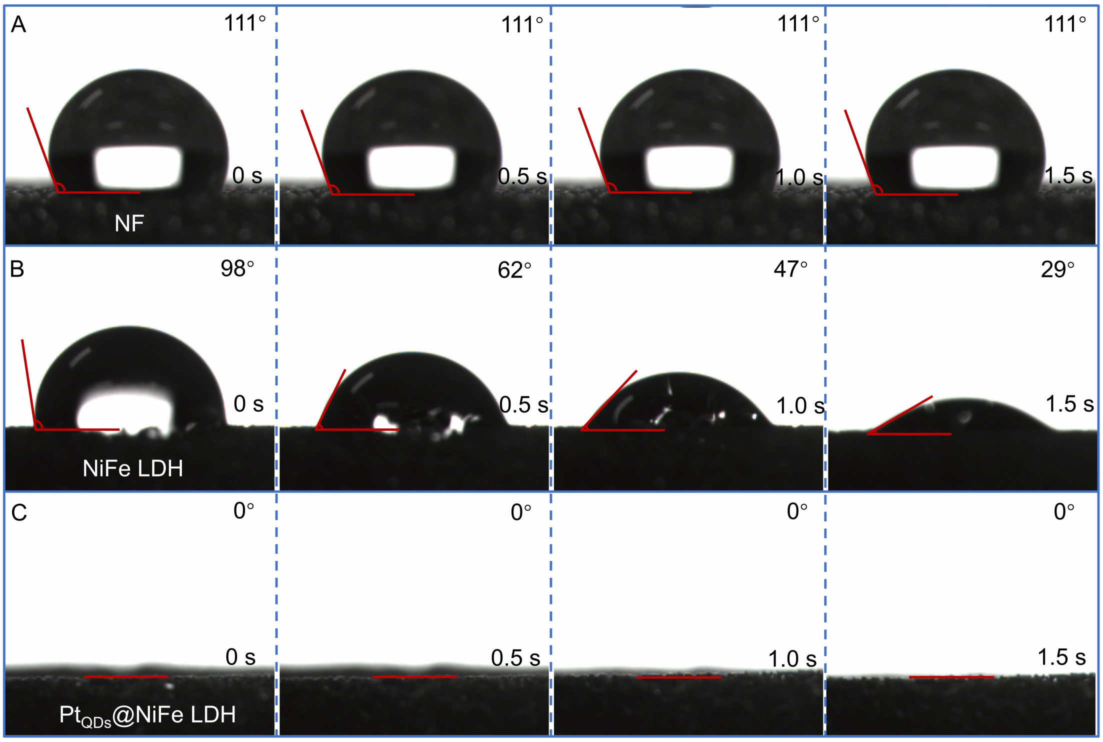

Supplementary Figure 7. The contact angles of (A) bare NF, (B) NiFe LDH and (C) Pt$_{QDs}$@NiFe LDH at different times.

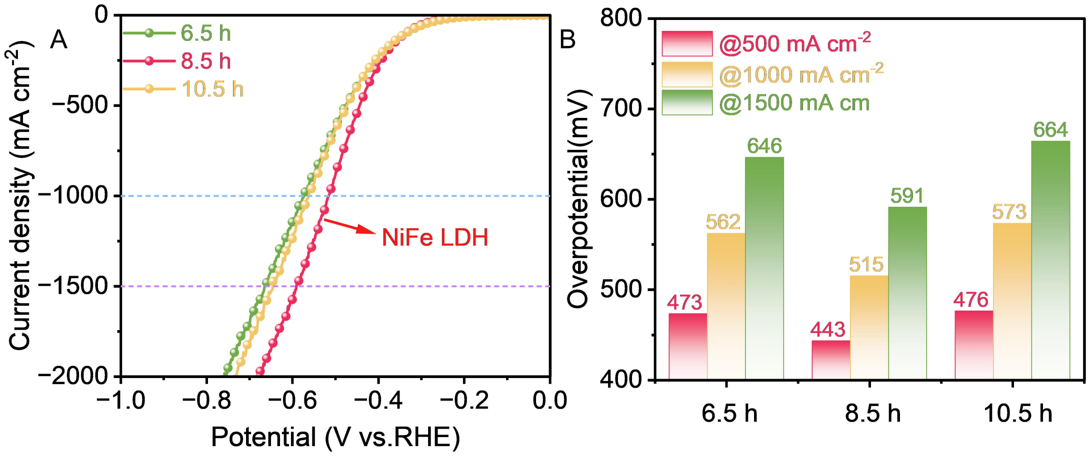

Supplementary Figure 8. (A) LSV curves of NiFe LDH-6.5, NiFe LDH-8.5 and NiFe LDH-10.5. (B) The overpotentials at 500, 1000 and 1500 mA cm^{-2}.

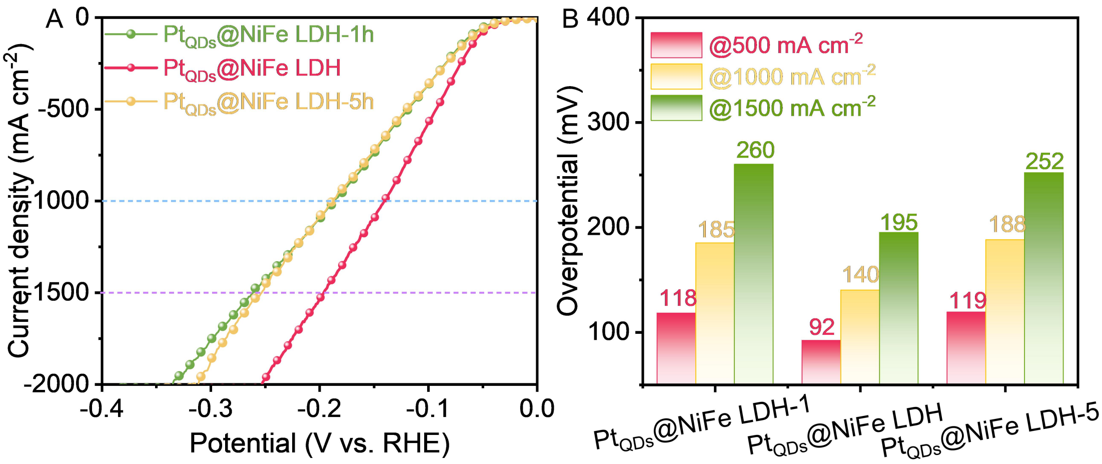

Supplementary Figure 9. (A) LSV curves of Pt$_{QDs}$@NiFe LDH-1, Pt$_{QDs}$@NiFe LDH and Pt$_{QDs}$@NiFe LDH-5. (B) The overpotentials at 500, 1000 and 1500 mA cm^{-2}.

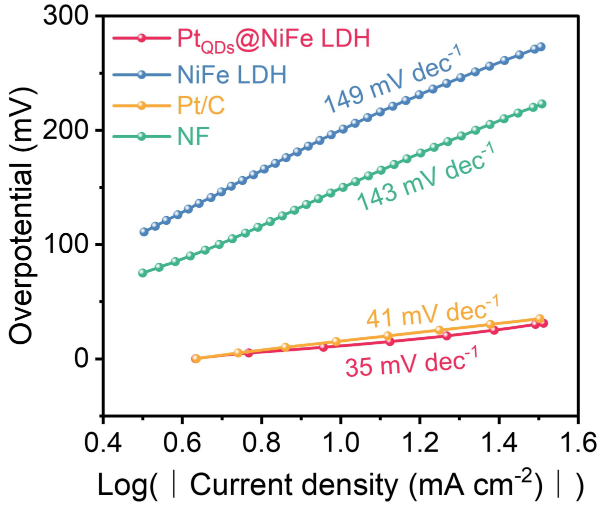

Supplementary Figure 10. Tafel slopes of Pt_{QDs}@NiFe LDH and other control samples**.**

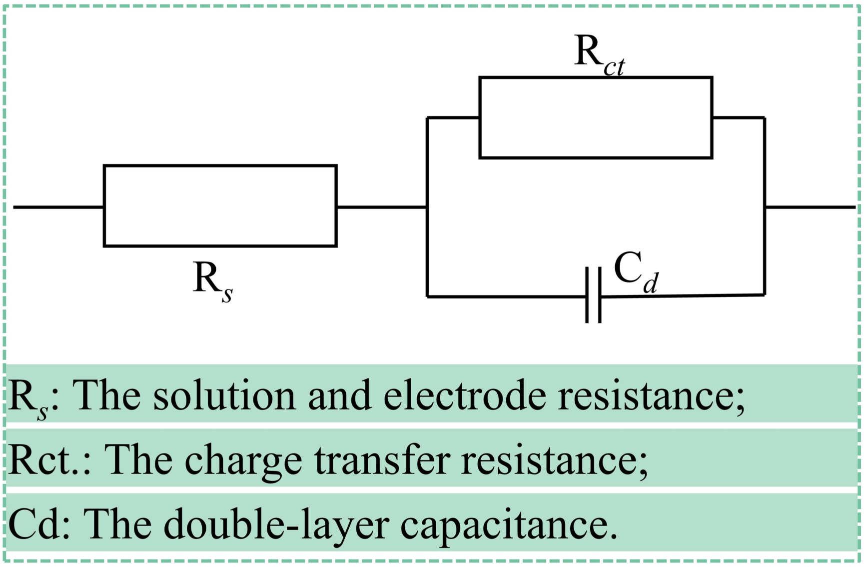

Supplementary Figure 11. The equivalent circuit diagram used for EIS analysis, which contains the solution and electrode resistance (R_s), charge transfer resistance (R_{ct}), and the double-layer capacitance (C_d).

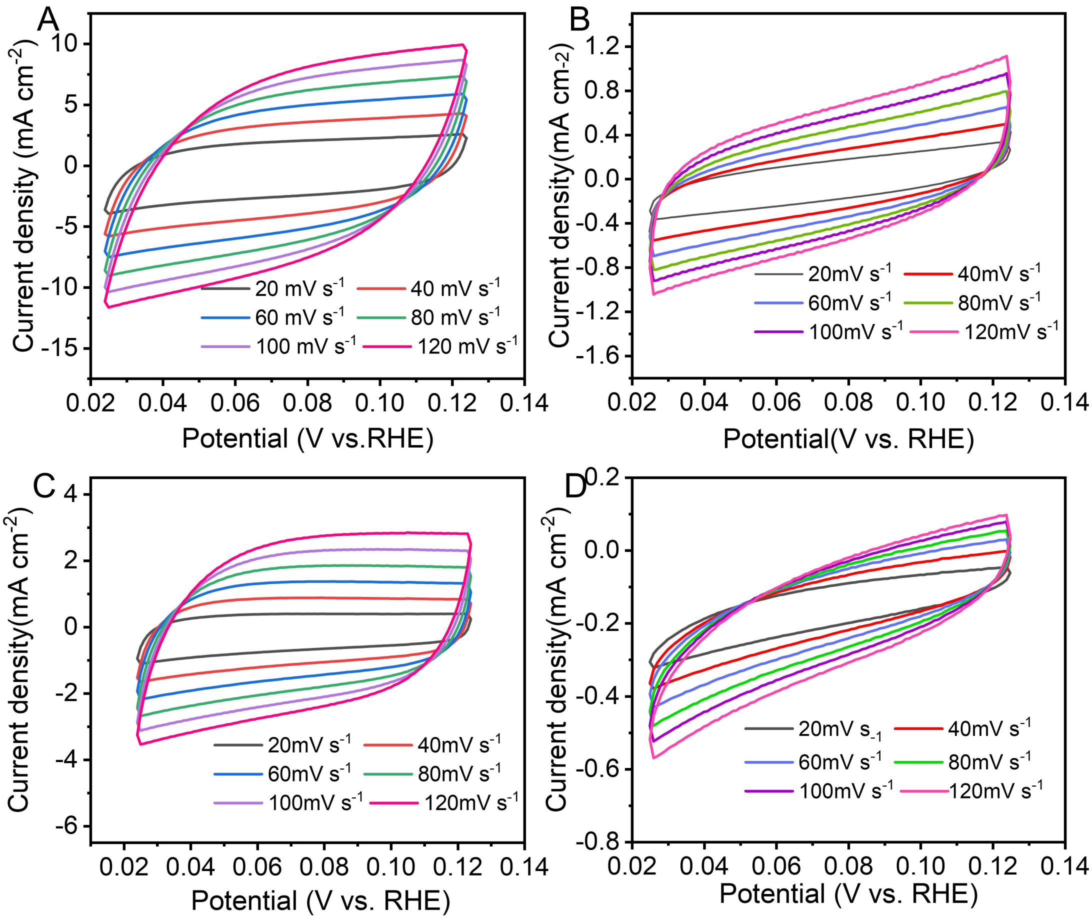

Supplementary Figure 12. CV curves of (A) Pt_{QDs}@NiFe LDH, (B) NiFe LDH, (C) Pt/C and (D) NF.

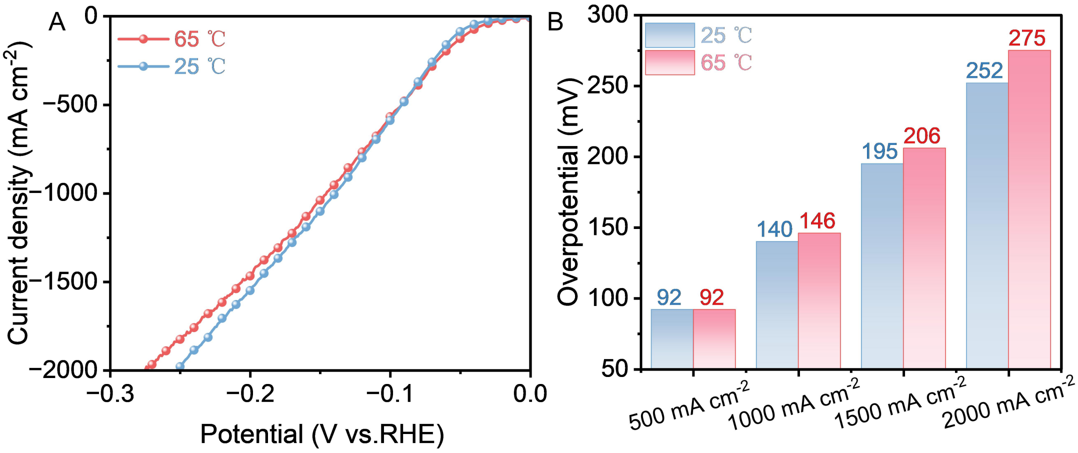

Supplementary Figure 13. (A) LSV curves of Pt_{QDs}@NiFe LDH at 25 °C and 65 °C. (B) The overpotentials at 500, 1000,1500 and 2000 mA cm^{-2}.

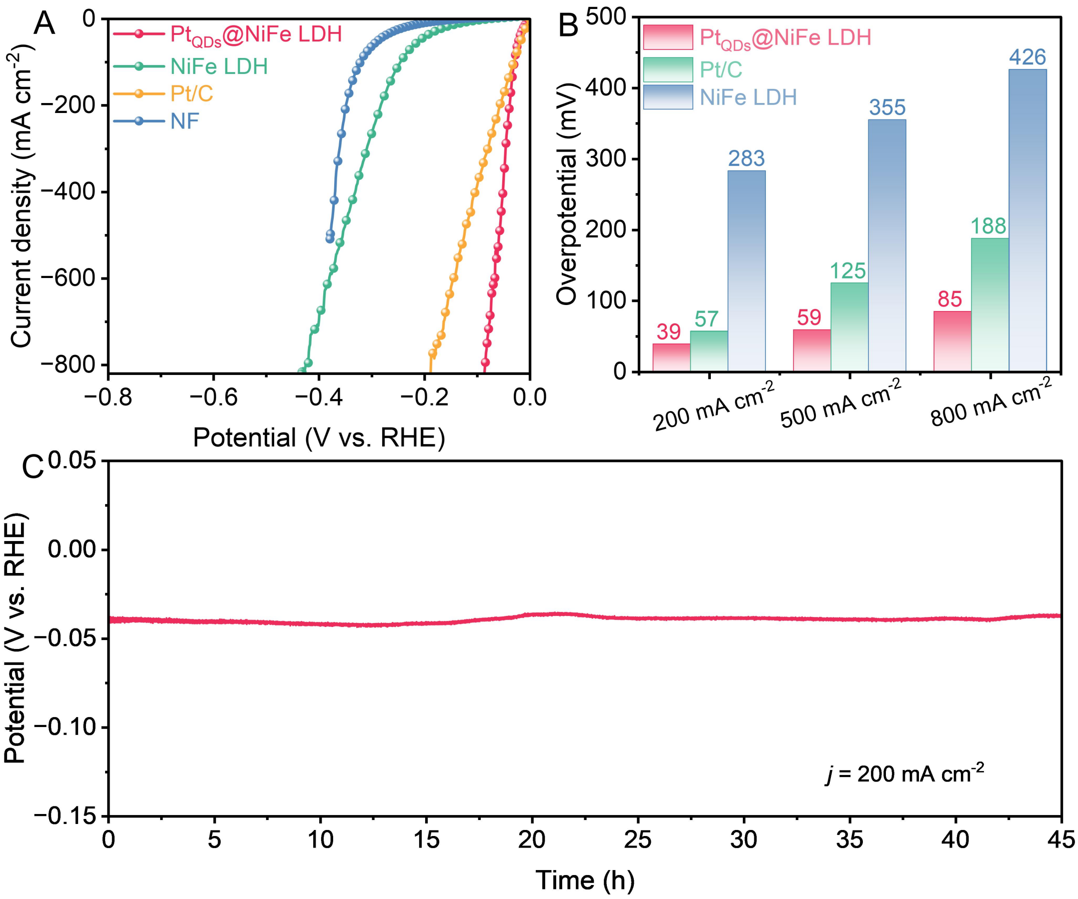

Supplementary Figure 14. HER performance tests in 0.5 M H_2SO_4 solution. (A) LSV curves. (B) The overpotentials at 500, 1000,1500 and 2000 mA cm^{-2}. (C) Stability test.

Supplementary Table 1. ICP result of Pt_{QDs}@NiFe LDH.

Elements	Content (wt%)
Ni	19.28
Fe	35.24
Pt	7.08

Supplementary Table 2. The exchange current densities are derived by Tafel plots.

Materials	Log|j, mA cm^{-2}|	exchange current density (j_0, mA cm^{-2})
Pt_{QDs}@NLDH	0.636	4.325
NiFe LDH	-0.127	0.746
Pt/C	0.634	4.305
NF	-0.064	0.863

Supplementary Table 3. Performance comparison of Pt_{QDs}@NiFe LDH with other electrocatalysts in 1 M KOH solution.

Catalysts	η_{500} (mV)	η_{1000} (mV)	Tafel slope (mV dec^{-1})	References
Pt_{QDs}@NiFe LDH	92	140	35	This work
Fe-Ni_3S_2/PNF-5	—	150	58.6	[5]
Ni_3N@2M-MoS_2	152	155	38.9	[6]
$Ni_{9.5}Co_{0.5}$-S-FeO_x	129	175	71.4	[7]
NiFe-P@NC	163	217	58	[8]
MoS_2/Mo_2C	—	220	43	[9]
$Ce_{0.2}$-CoP/Ni_3P@NF	195	225	55	[10]
Co_xP_v@NC	206	232	81.9	[11]
$Ni_{0.96}Co_{0.04}P$	—	249.7	49.6	[12]
MnO-CoP/NF	186	259.5	55.3	[13]
NiCo@C-NiCoMoO/NF	—	266	63.5	[14]
Ru_{SAs}/$Ni(OH)_2$@FeOOH	209	267	72	[15]
MnCo/NiSe	216	270	45.05	[16]
$Ni_{2(1-x)}Mo_{2x}P$	240	294	46.4	[17]
S-NiBDC	—	310	75	[18]
$Co_{0.59}Ni_{0.41}(OH)_2$@PANI/NF	—	310	36.41	[19]
Fe-Ni_2P@C/NF	294	313	45	[20]
Co_6Ni_4P/NF	—	336	61.24	[21]

Supplementary Table 4. Performance comparison of Pt_{QDs}@NiFe LDH (-) || NiFe LDH (+) with other electrocatalysts in 1 M KOH solution.

Catalysts	Cell Voltage (V) @ 100 mA cm^{-2}	References
Pt_{QDs}@NiFe LDH (-) || NiFe LDH (+)	1.54	This work
Pt/Mo-NiO_x/NMF (-) || NiFe-LDH/NF (+)	1.55	[22]
NiFeV@FeO_x/IF (-) || NiFeV@FeO_x/IF (+)	1.57	[23]
CoNiPeV/CFP (-) || CoNiPeV/CFP (+)	1.61	[24]
RuFe-SG-1 (-) || NiFe-LDH (+)	1.61	[25]
Pt@S–NiFe LDHs (-) || Pt@S–NiFe LDHs (+)	1.62	[26]
2% Ru-NCO (-) || 2% Ru-NCO (+)	1.65	[27]
NiPS/NF (-) || NiPS/NF (+)	1.66	[28]
Mn-NiCoP (-) || Mn- NiCoP (+)	1.69	[29]
CoNiFe-PS (-) || CoNiFe-PS (+)	1.69	[30]
$NiCe_{0.05}$/Fe@NM (-) || $NiCe_{0.05}$/Fe@NM (+)	1.70	[31]
NF10 (-) || NF10 (+)	1.73	[32]
RuNi-Fe_2O_3/IF (-) ‖ RuNi-Fe_2O_3/IF (+)	1.73	[33]
0.4-Co_2P/Ni_xP_y@NF (-) || 0.4-Co_2P/Ni_xP_y@NF (+)	1.74	[34]
Ru_{SA}-NiS_2-FeS_2 (-) || Ru_{SA}-NiS_2-FeS_2 (+)	1.74	[35]
Ni_3S_2-FeS/NF-2 (-) ||Ni_3S_2-FeS/NF-2 (+)	1.75	[36]

REFERENCES

1. Kresse G, Furthmüller J. Efficiency of ab-initio total energy calculations for metals and semiconductors using a plane-wave basis set. Comput. Mater. Sci. 1996; 6: 15-50. https://doi.org/https://doi.org/10.1016/0927-0256(96)00008-0.

2. Liu Q-L, Zhao Z-Y. DFT study on microstructures and electronic structures of Pt mono-/bi-doped anatase TiO_2 (101) surface. RSC Adv. 2015; 5: 17984-17992. https://doi.org/10.1039/C4RA12671H.

3. Parkinson GS, Novotny Z, Argentero G, Schmid M, Pavelec J, et al. Carbon monoxide-induced adatom sintering in a Pd-Fe_3O_4 model catalyst. Nat. Mater. 2013; 12: 724-728. https://doi.org/10.1038/nmat3667.

4. Torres E, Kaloni TP. Projector augmented-wave pseudopotentials for uranium-based compounds. Comput. Mater. Sci. 2020; 171: 109237. https://doi.org/https://doi.org/10.1016/j.commatsci.2019.109237.

5. Zhong B, Cheng B, Zhu Y, Ding R, Kuang P, et al. Hierarchically porous nickel foam supported Fe-Ni_3S_2 electrode for high-current–density alkaline water splitting. J. Colloid Interface Sci. 2023; 629: 846-853. https://doi.org/10.1016/j.jcis.2022.09.007.

6. Wu T, Song E, Zhang S, Luo M, Zhao C, et al. Engineering Metallic Heterostructure Based on Ni_3N and 2M-MoS_2 for Alkaline Water Electrolysis with Industry-Compatible Current Density and Stability. Adv. Mater. 2022; 34. https://doi.org/10.1002/adma.202108505.

7. Li S, Liu Y, Feng K, Li C, Xu J, et al. High Valence State Sites as Favorable Reductive Centers for High-Current-Density Water Splitting. Angew. Chem. Int. Ed. 2023; 62. https://doi.org/10.1002/anie.202308670.

8. Chen Z, Li Q, Xiang H, Wang Y, Yang P, et al. Hierarchical porous NiFe-P@NC as an efficient electrocatalyst for alkaline hydrogen production and seawater electrolysis at high current density. Inorg. Chem. Front. 2023; 10: 1493-1500. https://doi.org/10.1039/d2qi02703h.

9. Luo Y, Tang L, Khan U, Yu Q, Cheng H-M, et al. Morphology and surface chemistry engineering toward pH-universal catalysts for hydrogen evolution at high current density. Nat. Commun. 2019; 10. https://doi.org/10.1038/s41467-018-07792-9.

10. Zhang F, Wang X, Han W, Qian Y, Qiu L, et al. The Synergistic Activation of Ce-Doping and CoP/Ni3P Hybrid Interaction for Efficient Water Splitting at Large-Current-Density. Adv. Funct. Mater. 2022; 33. https://doi.org/10.1002/adfm.202212381.

11. Wang X, Liu X, Wu S, Liu K, Meng X, et al. Phosphorus vacancies enriched cobalt phosphide embedded in nitrogen doped carbon matrix enabling seawater splitting at ampere-level current density. Nano Energy 2023; 109. https://doi.org/10.1016/j.nanoen.2023.108292.

12. Lv X, Wan S, Mou T, Han X, Zhang Y, et al. Atomic-Level Surface Engineering of Nickel Phosphide Nanoarrays for Efficient Electrocatalytic Water Splitting at Large Current Density. Adv. Funct. Mater. 2022; 33. https://doi.org/10.1002/adfm.202205161.

13. Dong Y, Deng Z, Zhang H, Liu G, Wang X. A Highly Active and Durable Hierarchical Electrocatalyst for Large-Current-Density Water Splitting. Nano Letters 2023; 23: 9087-9095. https://doi.org/10.1021/acs.nanolett.3c02940.

14. Qian G, Chen J, Yu T, Luo L, Yin S. N-Doped Graphene-Decorated NiCo Alloy Coupled with Mesoporous NiCoMoO Nano-sheet Heterojunction for Enhanced Water Electrolysis Activity at High Current Density. Nano-Micro Lett. 2021; 13. https://doi.org/10.1007/s40820-021-00607-5.

15. Wang B, Sun H, Chen M, Zhou T, Zheng H, et al. Ru single-atom regulated $Ni(OH)_2$ nanowires coupled with FeOOH to achieve highly efficient overall water splitting at industrial current density. Chem. Eng. J. 2024; 479. https://doi.org/10.1016/j.cej.2023.147500.

16. Andaveh R, Sabour Rouhaghdam A, Ai J, Maleki M, Wang K, et al. Boosting the electrocatalytic activity of NiSe by introducing MnCo as an efficient heterostructured

electrocatalyst for large-current-density alkaline seawater splitting. Appl. Catal. B Environ. 2023; 325. https://doi.org/10.1016/j.apcatb.2022.122355.

17. Yu L, Mishra IK, Xie Y, Zhou H, Sun J, et al. Ternary $Ni_{2(1-x)}Mo_{2x}P$ nanowire arrays toward efficient and stable hydrogen evolution electrocatalysis under large-current-density. Nano Energy 2018; 53: 492-500. https://doi.org/10.1016/j.nanoen.2018.08.025.

18. Cheng F, Peng X, Hu L, Yang B, Li Z, et al. Accelerated water activation and stabilized metal-organic framework via constructing triangular active-regions for ampere-level current density hydrogen production. Nat. Commun. 2022; 13. https://doi.org/10.1038/s41467-022-34278-6.

19. Zhao S, Yin L, Deng L, Song J, Chang YM, et al. Inheritable Organic-Inorganic Hybrid Interfaces with π–d Electron Coupling for Robust Electrocatalytic Hydrogen Evolution at High-Current-Densities. Adv. Funct. Mater. 2022; 33. https://doi.org/10.1002/adfm.202211576.

20. Li D, Li Z, Zou R, Shi G, Huang Y, et al. Coupling overall water splitting and biomass oxidation via Fe-doped Ni_2P@C nanosheets at large current density. Appl. Catal. B Environ. 2022; 307. https://doi.org/10.1016/j.apcatb.2022.121170.

21. Wang K, Zhao R, Wang Z, Zhang X, Ouyang A, et al. Controlled tuning the morphology of CoNiP catalysts with ultra-high activity for water splitting at large current densities in alkaline medium. Appl. Surf. Sci. 2023; 626. https://doi.org/10.1016/j.apsusc.2023.157218.

22. Liu W, Li Y, Dou Y, Xu N, Wang J, et al. Light-driven assembly of Pt clusters on Mo-NiO_x nanosheets to achieve Pt/Mo-NiO_x hybrid with dense heterointerfaces and optimized charge redistribution for alkaline hydrogen evolution. J. Colloid Interface Sci. 2024; 655: 800-808. https://doi.org/10.1016/j.jcis.2023.11.065.

23. Yao H, Le F, Jia W, Cao Y, Sheng R, et al. Dual Electronic Modulations on NiFeV Hydroxide@FeO_x Boost Electrochemical Overall Water Splitting. Small 2023; 19. https://doi.org/10.1002/smll.202301294.

24. Sun S, Wang T, Qian K, Zhang H, Ji K, et al. Tailoring cation vacancies in Co, Ni phosphides for efficient overall water splitting. Int. J. Hydrogen Energy 2022; 47: 39731-39742. https://doi.org/10.1016/j.ijhydene.2022.09.156.

25. Liu X, Wang R, Chen Y, Zhang C, Li X, et al. Inhibitor-regulated corrosion strategy towards synthesizing cauliflower-like amorphous RuFe-hydroxides as advanced hydrogen evolution reaction catalysts. Int. J. Hydrogen Energy 2023; 48: 9333-9343. https://doi.org/10.1016/j.ijhydene.2022.12.040.

26. Lei H, Wan Q, Tan S, Wang Z, Mai W. Pt-Quantum-Dot-Modified Sulfur-Doped NiFe Layered Double Hydroxide for High-Current-Density Alkaline Water Splitting at Industrial Temperature. Adv. Mater. 2023. https://doi.org/10.1002/adma.202208209.

27. Zhang J, Lian J, Jiang Q, Wang G. Boosting the OER/ORR/HER activity of Ru-doped Ni/Co oxides heterostructure. Chem. Eng. J. 2022; 439. https://doi.org/10.1016/j.cej.2022.135634.

28. Wang H-Y, Ren J-T, Wang L, Sun M-L, Yang H-M, et al. Synergistically enhanced activity and stability of bifunctional nickel phosphide/sulfide heterointerface electrodes for direct alkaline seawater electrolysis. J. Energy Chem. 2022; 75: 66-73. https://doi.org/10.1016/j.jechem.2022.08.019.

29. Ma G, Ye J, Qin M, Sun T, Tan W, et al. Mn-doped NiCoP nanopin arrays as high-performance bifunctional electrocatalysts for sustainable hydrogen production via overall water splitting. Nano Energy 2023; 115. https://doi.org/10.1016/j.nanoen.2023.108679.

30. Yang N, Yang W, Yang X, Xiao X, Zhang L, et al. 2D/3D hierarchical and multi-heterostructured Co/Ni/Fe phosphosulfide as a highly efficient bifunctional electrocatalyst for overall water splitting. Int. J. Hydrogen Energy 2024; 56: 396-405. https://doi.org/10.1016/j.ijhydene.2023.12.221.

31. Yaseen W, Xie M, Yusuf BA, Meng S, Khan I, et al. Anchoring $Ni(OH)_2$-CeO_x Heterostructure on FeOOH-Modified Nickel-Mesh for Efficient Alkaline

Water-Splitting Performance with Improved Stability under Quasi-Industrial Conditions. Small 2024. https://doi.org/10.1002/smll.202403971.

32. Chen Y-F, Li J-H, Liu T-T, You S-H, Liu P, et al. Constructing robust NiFe LDHs–NiFe alloy gradient hybrid bifunctional catalyst for overall water splitting: one-step electrodeposition and surface reconstruction. Rare Met. 2023; 42: 2272-2283. https://doi.org/10.1007/s12598-022-02249-x.

33. Cui T, Zhai X, Guo L, Chi J-Q, Zhang Y, et al. Controllable synthesis of a self-assembled ultralow Ru, Ni-doped Fe_2O_3 lily as a bifunctional electrocatalyst for large-current-density alkaline seawater electrolysis. Chin. J. Catal. 2022; 43: 2202-2211. https://doi.org/10.1016/s1872-2067(22)64093-2.

34. Liu H, Zhang Y, Ge R, Cairney JM, Zheng R, et al. Tailoring the electronic structure of Ni_5P_4/Ni_2P catalyst by Co_2P for efficient overall water electrolysis. Appl. Energy 2023; 349. https://doi.org/10.1016/j.apenergy.2023.121582.

35. Ghising RB, Pan UN, Kandel MR, Dhakal PP, Sidra S, et al. Ruthenium single atoms implanted on NiS_2-FeS_2 nanosheet heterostructures for efficacious water electrolysis. J. Mater. Chem. A 2024; 12: 3489-3500. https://doi.org/10.1039/d3ta05630a.

36. Pan Z, Yaseen M, Kang Shen P, Zhan Y. Designing highly efficient 3D porous Ni-Fe sulfide nanosheets based catalyst for the overall water splitting through component regulation. J. Colloid Interface Sci. 2022; 616: 422-432. https://doi.org/10.1016/j.jcis.2022.02.085.